New Journal of Physics
The open-access journal for physics

# Reactive sputter deposition of $TiN_x$ films, simulated with a particle-in-cell/Monte Carlo collisions model

**E Bultinck[1,3], S Mahieu[2], D Depla[2] and A Bogaerts[1]**

[1] Research Group PLASMANT, Department of Chemistry, University of Antwerp, Universiteitsplein 1, 2610 Antwerp, Belgium
[2] Department of Solid State Sciences, Ghent University, Krijgslaan 281 (S1), 9000 Ghent, Belgium
E-mail: evi.bultinck@ua.ac.be

*New Journal of Physics* **11** (2009) 023039 (24pp)
Received 22 October 2008
Published 25 February 2009
Online at http://www.njp.org/
doi:10.1088/1367-2630/11/2/023039

**Abstract.** The physical processes in an $Ar/N_2$ magnetron discharge used for the reactive sputter deposition of $TiN_x$ thin films were simulated with a 2d3v particle-in-cell/Monte Carlo collisions (PIC/MCC) model. Cathode currents and voltages were calculated self-consistently and compared with experiments. Also, ion fractions were calculated and validated with mass spectrometric measurements. With this PIC/MCC model, the influence of $N_2/Ar$ gas ratio on the particle densities and fluxes was investigated, taking into account the effect of the poisoned state of the target.

[3] Author to whom any correspondence should be addressed.

## Contents



## 1. Introduction

Magnetron plasma sources have been intensively used since the 1970s [1], and nowadays play an important role in industry for the sputter deposition of thin metallic or compound films. Magnetron discharges are distinguished from conventional discharges by the presence of an externally applied magnetic field, apart from the applied electrical potential. This magnetic field is created by magnets placed behind the cathode. Due to their small Larmor radii, electrons rotate around the magnetic field lines, and are hence trapped in an area close to the cathode, where they can ionize the background gas atoms (e.g. argon). In this way, a discharge with enhanced ionization degree is created, which enables a lower working pressure. The electric field accelerates the ions towards the cathode target. After hitting the target, a collision cascade follows in the target, leading to a possible release of a surface atom. This process is called 'sputtering'. The sputtered atoms pass through the plasma and can be deposited on a substrate, forming a thin film. This whole process is hence denoted with the term 'sputter deposition', which is the main application of magnetron discharges.

When a reactive gas, like nitrogen or oxygen, is added to the Ar discharge, atoms originating from this reactive gas can react with the sputtered metal atoms on the substrate to form a metal nitride [2]–[9] or oxide layer [10]–[12], in a proces called 'reactive sputter deposition'. Certain metal nitride or oxide layers have interesting tribological properties [13]–[16], such as being anti-reflective, anti-static, hard, and corrosion and wear resistant. Some also have interesting electrical properties [4, 13].

Magnetron discharges for reactive sputter deposition purposes have been widely studied experimentally (a wide overview is presented in [17]). However, several experimental techniques can only be carried out at limited locations in the discharge (for instance not

always close to the target), and certain characteristics are hard to measure (for instance certain particle densities), or cannot be measured at all (for instance information on separate collision processes). Numerical modelling can overcome some of these experimental obstacles.

Different kinds of models exist to simulate gas discharges. Mostly, these models are subdivided into analytical, continuum and particle models. Analytical models [18] are based on simple analytical (mostly (semi-)empirical) formulae to describe the behaviour of macroscopic plasma characteristics, such as voltage and current. Their advantage is a short calculation time, but this is at the expense of accuracy, because approximations are used. Also, these models are mostly not general, meaning they only apply for a limited range of discharge conditions.

A continuum model [19] is based on the continuity equations and calculates, relatively fast, the electric field self-consistently. Hence, it is a very powerful modelling approach, if the 'local field approximation' is fulfilled, i.e. the charged particles' energies must be in equilibrium with the electric field. However, in a low-pressure discharge, such as a magnetron, this approximation is not valid, because the loss of energy caused by collisions is much smaller than the energy gain due to the electric field, especially for electrons. Furthermore, the complexity of the magnetic field makes a continuum model for magnetron discharges very inefficient [20].

Particle models do not suffer from the condition of continuum models, because all particles are followed individually. An example is a Monte Carlo (MC) model [21], that treats the collisions probabilistically, and calculates the particles' movements, starting from a known electric field distribution. This implies that the MC model is not self-consistent. However, this model can be coupled to a so-called particle-in-cell (PIC) model [22]–[24], which calculates all of the plasma characteristics in a self-consistent manner. The coupled model is named particle-in-cell/Monte Carlo collisions (PIC/MCC) model [23, 24]. PIC/MCC models calculate the entire discharge behaviour very accurately, however, a drawback is the longer calculation time, which is partially accounted for by representing real particles by a limited number of superparticles (SPs), and by weighting the SPs on a grid.

In the literature, the reactive magnetron sputter deposition was studied by means of simple analytical models, such as [25]–[27], and by MCC models [28]. A PIC/MCC model [29] was developed for an $Ar/O_2$ gas mixture. However, this PIC/MCC model does not take into account plasma–surface interactions, such as target sputtering, target poisoning and atom sticking, i.e. the sputter deposition process itself is not described. Moreover, these plasma–surface interactions influence all the calculated discharge characteristics [30, 31]. Secondly, the external circuit is not included in the model of [29]. Nevertheless, the external circuit appears to be essential in a PIC/MCC code for an accurate and correct description of magnetron discharges [32].

As summarized, a complete PIC/MCC model does not yet exist for an $Ar/N_2$ gas mixture in a magnetron discharge. However, an accurate modelling approach would be valuable as an extension for both experiments and existing simpler models. Therefore, to study the reactive magnetron sputter deposition process of $TiN_x$ layers, a PIC/MCC model is developed. Among other things, in the present work, the effect of $N_2/Ar$ gas ratio on the calculated discharge characteristics will be investigated.

## 2. Description of the experiments

A planar circular magnetron was used, on which a 50 mm diameter Ti target (3 mm thick and with 99.995% purity, Lesker) was clampled. The magnets placed behind the cathode have

a remanent magnetic field of 13 500 G, which generates a magnetic field with a maximum radial strength of 1040 G. The dimensions of the magnets were chosen in such a way that the area of the outer magnet ring was three times higher than the area of the inner magnet cylinder. Corresponding to the classification of Window and Savvides this magnet configuration corresponds to a slightly unbalanced type II magnetron [33].

The discharge was ignited in a pure Ar plasma at 1 Pa. For a discharge current of 0.2 A, a stable discharge voltage of 260 V was measured. Without interrupting the discharge and without changing the pumping speed, an additional $N_2$ flow was introduced in the vacuum chamber. This $N_2$ gas flow was controlled with a MKS mass flow controller. Due to the stepwise increase of the $N_2$ flow, a corresponding change in total pressure and discharge voltage was measured. The total pressure was measured with a capacitance gauge (Baratron, Pfeiffer Vacuum), whereas the discharge voltage was logged with a normal voltmeter. Since neither the Ar flow nor the pumping speed was changed, one can assume that the change in total pressure corresponds to the $N_2$ partial pressure.

Ion fractions were measured with a mass spectrometer. The composition of the ion flux towards the substrate was measured with an energy-resolved mass spectrometer (EQP500, Hiden Analytical) operated in the positive-ion mode, with the orifice at ground potential. First, an energy scan at mass 36 (an isotope of Ar) was performed to determine the most probable energy of the positive ions. At this fixed energy, the amount of positive ions with a mass of 14 ($N^+$), 28 ($N_2^+$), 36 ($Ar^+$) and 48 ($Ti^+$) was measured. Taking into account the mass abundances of these isotopes, the relative fluxes of these ions towards the orifice of the mass spectrometer could be calculated. However, due to a too strong influence of the mass spectrometer on the discharge, these measurements could not be performed at a target–orifice distance of 25 mm (as simulated). Therefore, these measurements were performed at a target–orifice distance of 70, 90, 110 and 130 mm. Since the measurements at 70 and 90 mm were comparable, one can assume that the relative fluxes at 20 mm will also be comparable with those measured at 70 mm.

## 3. Description of the magnetron in the model

The magnetron under study is based on a planar circular magnetron in a cylindrical chamber. Due to its cylindrical symmetry, the simulations can be carried out in 2d ($r$, $z$), as presented in [32]. An external resistance ($R_{ext}$) and voltage source ($V_{ext}$), which together form the external electrical circuit [32], are connected to the cathode, to create a direct current (dc). The other walls are grounded. In this manner, an electric field is generated in the discharge. In the model, the measured axisymmetric magnetic field was given as input (see section 2 above). In our simulations, we assume that the magnetron operates at room temperature (300 K), similar to the experiments. In order to study the effect of the $N_2$/Ar gas ratio, the Ar partial pressure was kept constant at 1 Pa for all the calculations, whereas the partial pressure of $N_2$ was varied, according to the measured values (see section 2 above, and section 5.1 below).

## 4. Description of the model

As mentioned before, because of the cylindrical symmetry, the magnetron can be described in a two-dimensional space, i.e. ($r$, $z$) coordinates. However, all three velocity components must be taken into account in order to describe properly the electron gyration around the magnetic field lines, and to satisfy the energy conservation. The model developed in the present work

is therefore a so-called 2d3v PIC/MCC model, i.e. two dimensional in space (2d) and three dimensional in velocity (3v). The outlines of this method are given in [20], [22]–[24], [32, 34], the flow chart of the model is presented in [32]. The particle movement is simulated with the PIC method (section 4.1), the collisions are treated with the MCC module (section 4.2), and plasma–surface interactions, such as sputtering, electron emission, species reflection and the effect of poisoning, are accounted for (section 4.3).

### *4.1. PIC method*

The real particles in the discharge are represented by a limited ensemble of so-called SPs. Each SP has a weight factor $W$ that specifies the number of real particles it represents. This is done to reduce the computation time. The program starts with an initial number of SPs and fixed number densities of the electrons, the $Ar^+$ ions, the $N^+$ ions and the $N_2^+$ ions, i.e. 50 000 SPs for electrons, 40 000 SPs for ions and a number density of $10^{15}\,m^{-3}$. Initially, the SPs are uniformly distributed and are assumed to have Maxwellian velocities.

Instead of calculating the field quantities on every SP itself, they are calculated on a grid to reduce the calculation time. The SPs are first-order weighted [22] to obtain a charged particle density landscape on the $(r, z)$ grid, with $\Delta r = 0.5$ mm and $\Delta z = 0.1$ mm.

The electrical potential $V$ is calculated from the charge density using the Poisson equation. However, in order to simplify the solution of this equation, we use the superposition principle, so that the electrical potential can be presented as the sum of the potential only due to the space charge ($V_P$) and the potential only due to the cathode voltage ($U_0$):

$$V = V_P + U_0 V_L, \tag{1}$$

where $V_L$ is the dimensionless potential caused by an applied voltage with magnitude 1 V [35].

$V_P$ can be found as a solution of the Poisson equation, which in $(r, z)$ coordinates reads

$$\frac{1}{r}\frac{\partial}{\partial r} r \frac{\partial V_p}{\partial r} + \frac{\partial}{\partial z}\frac{\partial V_p}{\partial z} = -\frac{q}{\epsilon_0}(n_i - n_e), \tag{2}$$

with $q$ being the elementary charge, $\epsilon_0$ the dielectric constant and $n_i$ and $n_e$ the ion and electron densities, respectively. Equation (2) can be solved with zero-potential boundary conditions, i.e. $V_P = 0$ at the surfaces $z = 0$ and $z_{max}$ and $r = r_{max}$. Due to the cylindrical symmetry, the physical boundary condition at $r = 0$ is

$$\left(\frac{\partial V_P}{\partial r}\right)_{r=0} = 0. \tag{3}$$

In [32], it is shown how the voltage drop between the electrodes ($U_0$) is calculated, resulting from the coupling of the external circuit to the plasma. In the simulation, an external circuit consisting of a constant external voltage source and resistor is applied to limit the plasma current to the desired current–voltage ($I$–$V$) regime. This external circuit is explained in [32].

$V_L$ is the solution of the Laplace equation

$$\Delta V_L = 0, \tag{4}$$

with the applied potential boundary condition, i.e. $V_L = 1$ at the cathode surface and $V_L = 0$ at the grounded walls. Moreover, in the gap between the cathode and the grounded wall at $z = 0$, $V_L$ is assumed to decay linearly from 1 to 0 with the distance from the cathode. The Laplace equation needs to be solved only at the beginning of the simulation, which simplifies

and accelerates the calculation of the Poisson equation. Equations (2) and (4) are discretized using a standard five-point stencil [36] and solved on the grid.

The electric field $E$ is obtained as

$$\mathbf{E} = -\nabla V. \tag{5}$$

This equation is discretized by the central finite difference method. On the boundaries, forward or backward differencing is applied.

This new electric field, together with the applied electric and magnetic fields, moves the SPs, according to Newton's equations of motion:

$$\begin{aligned} m\frac{\mathrm{d}\mathbf{v}}{\mathrm{d}t} &= q\,(\mathbf{E}+\mathbf{v}\times\mathbf{B})\,, \\ \frac{\mathrm{d}\mathbf{x}}{\mathrm{d}t} &= \mathbf{v}, \end{aligned} \tag{6}$$

where $m$ is the mass, $\mathbf{v}$ the velocity, $q$ the charge, $\mathbf{x}$ the position, $\mathbf{E}$ the electric field and $\mathbf{B}$ the magnetic field. These equations are discretized using the central finite difference method, resulting in the so-called leap-frog method [22]. The $\mathbf{v}\times\mathbf{B}$ rotation term is treated according to the algorithm suggested by Boris [37].

After these new positions and velocities are obtained, the procedure is repeated, until the plasma is at steady state.

### *4.2. MCC module*

The particle collisions are treated in the MCC module. At the middle of each time step, the probability of the $k$th collision type is

$$P_k = 1 - \exp\left(-\Delta t \cdot v \cdot n_{\mathrm{tar}} \cdot \sigma_k\left(E_{\mathrm{i}}\right)\right), \tag{7}$$

with $n_{\mathrm{tar}}$ being the density of the target species and $\sigma_k(E_{\mathrm{i}})$ the collision cross section as a function of the energy of the incident particle $E_{\mathrm{i}}$. This probability is compared to a random number, uniformly distributed in the interval [0, 1]. If this random number is smaller, then the collision takes place, and the particles receive new positions and velocities according to the collision type. Details about their treatment for a magnetron discharge in argon are given in [23, 34]. The list of the considered collisions in the $Ar/N_2$ discharge, and their rate constants and references to their cross sections is given in table 1. Besides elastic collisions with Ar atoms, and electron impact ionization and excitation of Ar (ground state and metastable atoms), also electron impact ionization, excitation (to four different excited levels), dissociative ionization and dissociation of the $N_2$ gas molecules are included. Ionization of N is not considered, because N has a lower density, and hence its ionization is less important. Also, the density of $N^+$ is low, so recombination of $N^+$ is also not included. Elastic collisions of electrons with $N_2$ are also omitted, due to the lower density of $N_2$, so the momentum change of the electrons by elastic collisions with $N_2$ is small compared with Ar. As far as the heavy particle collisions are concerned, elastic scattering of $Ti^+$ with $N_2$ and N is included, because, in constrast to electrons, a considerable amount of energy is transferred. Charge transfer of $Ar^+$ with $N_2$ is included, due to its very high rate constant. The model also contains elastic and charge transfer $N(_2)^+$ collisions with Ar, $N_2$ and N.

Note that not only electrons, $Ar^+$ ions, $N^+$ ions and $N_2^+$ ions, which are assumed to be present from the beginning, are included in the model. Also fast Ar atoms (that originate

**Table 1.** List of the considered collisions and their corresponding cross sections ($m^2$) or rate constants ($m^3\,s^{-1}$). 'LH' denotes the Langevin–Hasse collision treatment. '(a)' refers to assumed rate constants based on similar reactions, due to lack of data in the literature.

| | | | | |
|---|---|---|---|---|
| $e^-$ collisions | | | | |
| (1) | $e^- + Ar \rightarrow e^- + Ar$ | Elastic scattering | $\sigma(E)$ | [57] |
| (2) | $e^- + Ar \rightarrow 2e^- + Ar^+$ | Electron-impact ionization | $\sigma(E)$ | [58] |
| (3) | $e^- + Ar \rightarrow e^- + Ar^*_m$ | Electron-impact excitation | $\sigma(E)$ | [59] |
| (4) | $e^- + Ar \rightarrow e^- + Ar^*$ | Electron-impact excitation | $\sigma(E)$ | [60] |
| (5) | $e^- + Ar^*_m \rightarrow 2e^- + Ar^+$ | Electron-impact ionization | $\sigma(E)$ | [61] |
| (6) | $e^- + Ar^*_m \rightarrow e^- + Ar^*$ | Electron-impact excitation | $\sigma(E)$ | [62] |
| (7) | $e^- + Ti \rightarrow 2e^- + Ti^+$ | Electron-impact ionization | $\sigma(E)$ | [63] |
| (8) | $e^- + N_2 \rightarrow 2e^- + N_2^+$ | Electron-impact ionization | $\sigma(E)$ | [64] |
| (9) | $e^- + N_2 \rightarrow e^- + N_2^*$ | Electron-impact excitation to $A^3\sigma_u^+$ | $\sigma(E)$ | [64] |
| (10) | $e^- + N_2 \rightarrow e^- + N_2^*$ | Electron-impact excitation to $B^3\Pi$ | $\sigma(E)$ | [64] |
| (11) | $e^- + N_2 \rightarrow e^- + N_2^*$ | Electron-impact excitation to $C^3\Pi$ | $\sigma(E)$ | [64] |
| (12) | $e^- + N_2 \rightarrow e^- + N_2^*$ | Electron-impact excitation to $a^1\Pi_g$ | $\sigma(E)$ | [64] |
| (13) | $e^- + N_2 \rightarrow 2e^- + N^+ + N$ | Dissociative ionization | $\sigma(E)$ | [65] |
| (14) | $e^- + N_2 \rightarrow e^- + N + N$ | Dissociation | $\sigma(E)$ | [64] |
| (15) | $e^- + N_2^+ \rightarrow N + N$ | Dissociative recombination | $k = 4.8 \times 10^{-13}\sqrt{300/T_e}$ | [66] |
| $Ar^+$ collisions | | | | |
| (16) | $Ar^+ + Ar \rightarrow Ar^+ + Ar_f$ | Elastic scattering | $\sigma(E)$ | [38] |
| (17) | $Ar^+ + Ar \rightarrow Ar_f + Ar^+$ | Charge transfer | $\sigma(E)$ | [38] |
| (18) | $Ar^+ + Ar \rightarrow 2Ar^+ + e^-$ | Ion-impact ionization | $\sigma(E)$ | [67] |
| (19) | $Ar^+ + Ar \rightarrow Ar^+ + Ar^*_m$ | Ion-impact excitation | $\sigma(E)$ | [67] |
| (20) | $Ar^+ + Ti \rightarrow Ar + Ti^+$ | Charge transfer | $k = 6.61 \times 10^{-17}$ | [68] |
| (21) | $Ar^+ + N_2 \rightarrow Ar + N_2^+$ | Charge transfer | $k = 4.45 \times 10^{-16}$ | [69] |
| $Ar^*_m$ collisions | | | | |
| (22) | $Ar^*_m + Ar^*_m \rightarrow Ar + Ar^+ + e^-$ | Metastable–metastable collision | $k = 6.4 \times 10^{-16}$ | [70, 71] |
| (23) | $Ar^*_m + Ti \rightarrow Ar + Ti^+ + e^-$ | Penning ionization of Ti | $\sigma = 4.93 \times 10^{-19}$ | [72] |
| (24) | $Ar^*_m + Ar \rightarrow Ar + Ar$ | Two-body collision with Ar | $k = 2.3 \times 10^{-21}$ | [73] |
| $Ar_f$ collisions | | | | |
| (25) | $Ar_f + Ar \rightarrow Ar_f + Ar_f$ | Elastic scattering | $\sigma(E)$ | [74] |
| (26) | $Ar_f + Ar \rightarrow Ar + Ar^+$ | Atom-impact ionization | $\sigma(E)$ | [67] |
| (27) | $Ar_f + Ar \rightarrow Ar_f + Ar^*_m$ | Atom-impact excitation | $\sigma(E)$ | [75] |
| $Ti^+$ collisions | | | | |
| (28) | $Ti^+ + Ar \rightarrow Ti^+ + Ar$ | Elastic scattering | $\sigma = 6 \times 10^{-20}$ | [76] |
| (29) | $Ti^+ + N_2 \rightarrow Ti^+ + N_2$ | Elastic scattering | $\sigma(E)$ | LH |
| (30) | $Ti^+ + N \rightarrow Ti^+ + N$ | Elastic scattering | $\sigma(E)$ | LH |
| Ti collisions | | | | |
| (31) | $Ti_f + Ar \rightarrow Ti + Ar_f$ | Elastic scattering | $\sigma = 6 \times 10^{-20}$ | [76] |
| (32) | $Ti + N \rightarrow TiN$ | Attachment | Only at the walls (SC) | Section 4.3 |

**Table 1.** Continued.

| | | | | |
|---|---|---|---|---|
| $N^+$ collisions | | | | |
| (33) | $N^+ + Ar \rightarrow N^+ + Ar_f$ | Elastic scattering | $\sigma(E)$ | LH |
| (34) | $N^+ + Ar \rightarrow N + Ar^+$ | Charge transfer | $k = 4 \times 10^{-17}$ | (a) |
| (35) | $N^+ + N_2 \rightarrow N^+ + N_2$ | Elastic scattering | $\sigma(E)$ | LH |
| (36) | $N^+ + N_2 \rightarrow N + N_2^+$ | Charge transfer | $k = 4 \times 10^{-17}$ | (a) |
| (37) | $N^+ + N \rightarrow N^+ + N_f$ | Elastic scattering | $\sigma(E)$ | LH |
| (38) | $N^+ + N \rightarrow N_f + N^+$ | Charge transfer | $k = 4 \times 10^{-17}$ | (a) |
| $N_2^+$ collisions | | | | |
| (39) | $N_2^+ + Ar \rightarrow N_2^+ + Ar$ | Elastic scattering | $\sigma(E)$ | LH |
| (40) | $N_2^+ + Ar \rightarrow N_2 + Ar^+$ | Charge transfer | $k = 1 \times 10^{-17}$ | (a) |
| (41) | $N_2^+ + N_2 \rightarrow N_2^+ + N_2$ | Elastic scattering | $\sigma(E)$ | LH |
| (42) | $N_2^+ + N_2 \rightarrow N_2 + N_2^+$ | Charge transfer | $k = 1 \times 10^{-17}$ | (a) |
| (43) | $N_2^+ + N \rightarrow N_2^+ + N$ | Elastic scattering | $\sigma(E)$ | LH |
| (44) | $N_2^+ + N \rightarrow N_2 + N^+$ | Charge transfer | $k = 1 \times 10^{-17}$ | (a) |

from elastic collisions, including symmetric charge transfer collisions, with $Ar^+$ ions [38], i.e. reactions (16) and (17) from table 1), metastable Ar atoms, fast Ti atoms, $Ti^+$ ions and fast N atoms, created out of the initial species (by plasma reactions or by sputtering) are considered. Slow Ti and N atoms are described in the model with balance equations (see section 4.3).

Some cross sections of ion–neutral collisions are described with the Langevin–Hasse model [39, 40], assigned 'LH' in table 1:

$$\sigma_k = \left(\frac{\pi \alpha_p e^2}{\epsilon_0 \mu}\right)^{1/2} \beta_\infty^2 g^{-1}, \tag{8}$$

where $\alpha_p$ is the polarizability, $e$ the electron charge, $\epsilon_0$ the dielectric constant of vacuum, $\mu$ the reduced mass, $g = |v_i - v_n|$ the relative precollision velocity, with $v_i$ and $v_n$ the ion and neutral velocities, respectively, and $\beta_\infty$ is the value of the dimensionless impact parameter $\beta$, for which the deflection angle is negligibly small [41]. This value is set to 3 for Ar, $N_2$ and N [40]. The polarizability for Ar is $11.08a_0^3$ [42], $18.24a_0^3$ for $N_2$ [43] and $7.5a_0^3$ for N [42], where $a_0$ is the Bohr radius.

### *4.3. Plasma–surface interactions, implemented in the model*

Since magnetron discharges are mainly applied as sputter devices, the sputtering of the target is included in the model. This is done by calculating the sputter yield $Y$, each time an ion or atom hits the cathode surface. The sputter yield for an incident particle i with energy $E_i$ is described by the empirical formula of Matsunami [44]

$$Y(E_i) = 0.42 \frac{\alpha Q K s_n(E_i)}{U_s (1 + 0.35 U_s s_e(E_i))} \left[1 - (E_{th}/E_i)^{1/2}\right]^{2.8}, \tag{9}$$

where $U_s$ is the sublimation energy of the cathode, $E_{th}$ the threshold energy and the other parameters are properties of the cathode material, as described in [44].

The sputtered Ti atoms (and N, in the case of a poisoned target, see section 4.4) are followed with the PIC/MCC method until they are thermalized in order to reduce the computation time. However, the Ti (and N) atom density is important in picturing the deposition process. Therefore a compromise is found between computational effort and accuracy in treating the thermalized Ti (and N) atoms as a fluid, and hence their density $n_{\text{slow}}(r, z)$ is calculated with the diffusion equation

$$\frac{\partial n_{\text{slow}}}{\partial t} - D\Delta n_{\text{slow}}(r, z) = r_{\text{prod}}(r, z) - r_{\text{loss}}(r, z), \tag{10}$$

where $D$ is the diffusion coefficient of Ti or N atoms in Ar gas, and $r_{\text{prod}}$ and $r_{\text{loss}}$ are the production and loss rates, respectively, of the Ti or N atoms. The production mechanisms of slow Ti atoms are defined by transfer from the fast (sputtered) Ti atoms, i.e. thermalization by elastic collisions with Ar (reaction (31) from table 1) and thermalization at the walls, whereas the loss mechanisms of slow Ti atoms are electron impact ionization (reaction (7) from table 1), and Penning ionization (reaction (23) from table 1). Slow N atoms are produced by thermalization of fast N atoms at the walls, as well as by thermalization of these fast N atoms by elastic collisions with $Ti^+$ ions (reaction (30)), $N^+$ ions (reaction (37)) and $N_2^+$ ions (reaction (43)). Other production mechanisms are dissociative ionization (reaction (13)) and dissociation of $N_2$ gas molecules (reaction (14)), and dissociative recombination of $N_2^+$ (reaction (15)). Charge-transfer reactions of $N^+$ ions can also cause the creation of slow N atoms, i.e. with Ar gas atoms (reaction (34)), $N_2$ gas molecules (reaction (36)), N atoms (reaction (38)). Slow N atoms can be lost by elastic collisions with $N^+$ ions, including charge transfer, and by charge transfer with $N_2^+$ ions (reaction (44)), because these processes give rise to the creation of fast N atoms.

The diffusion coefficient (in $m^2\,s^{-1}$) is calculated from the rigid sphere approximation [45]

$$D = 2.628 \times 10^{-7} \frac{\sqrt{T^3\,(M_1 + M_2)\,/2M_1M_2}}{pd_{12}^2}, \tag{11}$$

where $T$ is the gas temperature (K), $M_1$ and $M_2$ are the masses of Ti (or N), and Ar ($g\,mole^{-1}$), $p$ is the pressure (atm), and $d_{12}$ is the collision diameter ($10^{-10}$ m), given by $(d_1 + d_2)/2$. The collision diameter of Ti is $2.684 \times 10^{-10}$ m [46], $3.298 \times 10^{-10}$ m for N [47], and $3.542 \times 10^{-10}$ m for Ar [47].

The second plasma–surface interaction taken into account is ion- or atom-induced secondary electron emission, characterized by the secondary electron emission coefficient (SEEC). The SEEC describes the number of secondary electrons produced by an atom or ion hitting the cathode surface. Note that secondary electron emission at the other walls is less important, so it is not included. Unfortunately, a wide range of different SEEC values are reported for ion bombardement of Ti (from 0.075 [48] to 0.148 [49]). Moreover, some of these values describe the effective secondary electron yield, which is dependent on both SEEC and reflection coefficient (RC) [50] (see below). Therefore, the exact SEEC is not known.

Another plasma–surface interaction regards an electron striking a wall, after which it can be reflected or adsorbed, characterized by the RC. In magnetrons, the electron density near the cathode is much higher than at the other walls, so only interaction of electrons with the cathode surface is important. The RC is, however, hard to measure and to our knowledge no values are reported in the literature. Since both the RC and the SEEC directly influence the cathode current and voltage [51], they are slightly adapted in the model, so that the calculated currents and voltages can be compared with experimental values. Note, however, that these coefficients

were kept the same for the different $I$–$V$ combinations investigated for sputtering of Ti in pure Ar.

Similarly to electrons, heavy particles can also be reflected or adsorbed when hitting a wall, depending on the sticking coefficient (SC). The SC of a reactive N atom is mostly assumed to be 1 [26], whereas the SC of Ti is found to be dependent on target–substrate distance [52]. In accordance to these reported values [52], an $SC_{Ti}$ of 0.5 is chosen in our model. The SC of the background gases is assumed in the model to be 0. For Ar being an inert gas, a zero sticking approximation is justified. The zero sticking for $N_2$, on the other hand, is chosen based on the following: the partial pressure of $N_2$ is used in the code as measured by experiment. In the simulation, this constant partial pressure corresponds to the assumption of a zero effective SC for $N_2$. Moreover, the SC of $N_2$ is very low, and its influence on the calculated $N_2$ density is therefore negligible, which also justifies the assumption.

When a heavy particle is reflected, a distinction is made between elastic and inelastic reflections depending on the thermal accommodation coefficient, defined as

$$\alpha = \frac{E_i - E_r}{E_i - E_w}, \tag{12}$$

where $E_i$ is the mean energy of the incoming particles, $E_r$ the mean energy of the reflected particles and $E_w$ the mean energy of the reflected particles in thermal equilibrium with the wall ($2kT_w$). This means that if $E_r = E_w$, all the energy of the incoming particle is transfered to the wall, and an inelastic reflection occurred. In this case, $\alpha$ is equal to 1. If, however, $E_r = E_i$ then the energy is conserved, and an elastic reflection occurred. In this case $\alpha$ is 0. In the simulation, $\alpha$ is assumed to be 0.5 [53], and a random number is generated. When the random number is lower than $\alpha$, an inelastic reflection occurs, and if the random number is higher than $\alpha$, an elastic reflection occurs.

### *4.4. Effect of poisoning on the plasma–surface interactions and on their implementation in the model*

When a reactive gas, like nitrogen, is added to the argon background gas, $N(_2)^+$ ions can be implanted in the Ti target, nitrogen molecules and atoms can be chemisorbed at the target surface, and chemisorbed species can be knock-on implanted into the target. Subsequently, they react with the target atoms, to form a $TiN_x$ layer, similar to the mechanism in oxygen [30]. This surface modification process is called 'poisoning', and influences the plasma–target interactions (i.e. sputtering and secondary electron emission), and therefore all of the plasma properties. The transition from the so-called metallic to poisoned condition happens via a hysteresis [30, 31]. In the present work, we used $N_2$ gas flows for which the target is completely in poisoned mode, in order to avoid (i) the simulation of the hysteresis and (ii) having to deal with a partially reacted Ti target.

Both Ti and N atoms can be sputtered from a poisoned $TiN_x$ target, but their sputter yield is lower than for a metallic Ti target. According to the values reported in [26], the sputter yield of Ti from a fully poisoned target is lowered with a factor of 6.4 compared with the sputter yield of Ti from a metallic target. On the other hand, the sputter yield of N from a fully poisoned target is 4 times higher, compared to the sputter yield of Ti from a fully poisoned target. These changes in sputter yields for the poisoned target apply to all of the bombarding species (i.e. $Ar^+$, $Ar_f$, $N_2^+$, $N^+$ and $Ti^+$; see later, section 5.4 and tables 2 and 3).

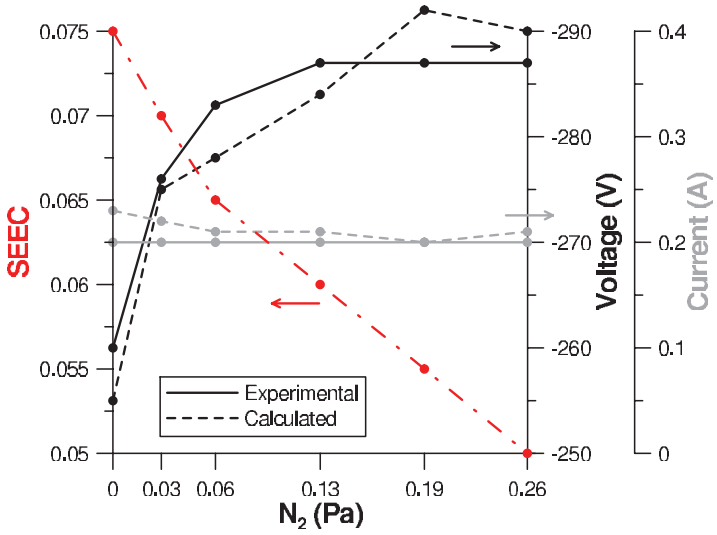


**Figure 1.** Measured and calculated values of the cathode potentials and currents as a function of $N_2$ partial pressure, at an Ar partial pressure of 1.0 Pa, an external voltage of −600 V, and an external resistance ($R_{ext}$) of 1500 Ω. The SEEC values used in the model for different $N_2$ partial pressures are also indicated. They drop from 0.075 in the case of pure Ar to 0.05 for the case of 0.26 Pa $N_2$.

Moreover, due to the target surface modification the SEEC is altered that results in a target voltage change [50]. In the model, the poisoning of the target is therefore described by changing the SEEC value, depending on the $N_2$ gas flow. The SEEC value is adjusted, in accordance with the range reported in [50] (see values below).

## 5. Results and discussion

### *5.1. Input values and calculated I–V characteristics*

In our calculations, an RC of 0.1 and an SEEC of 0.075 yielded calculated *I–V* values in good agreement with the experimental data in pure Ar. Starting from these coefficients, an $Ar/N_2$ mixture is evaluated in a constant current regime of 0.2 A (accomplished with $V_{ext} = -600$ V and $R_{ext} = 1500\ \Omega$). The applied magnetic field has a maximum radial magnetic field strength of 1040 G. To study the effect of the $N_2/Ar$ gas proportion, the Ar partial pressure is kept constant at 1 Pa for all calculations, whereas the $N_2$ partial pressure is increased as 0.03, 0.06, 0.13, 0.19 and 0.26 Pa. Under these conditions, the target is always fully poisoned, so that the hysteresis behaviour can be avoided. To summarize, only the partial pressures of the Ar and $N_2$ gases, $V_{ext}$ and $R_{ext}$, the magnetic field, the SC, RC and SEEC (discussed in sections 4.3 and 4.4), and the cross sections and rate coefficients of the various collisions in the plasma (see table 1) are input values in the model. All the other plasma characteristics, including the results presented below, are calculated self-consistently.

The SEEC alters as a consequence of poisoning, and in the case of a $TiN_x$ target, the SEEC decreases [50]. Note that the SEEC values applied in the model comprise the SEEC values of all different incident species, to avoid complicating the model with different uncertain parameters. From figure 1, it is clear that the overall SEEC is lowered in the model with increasing the

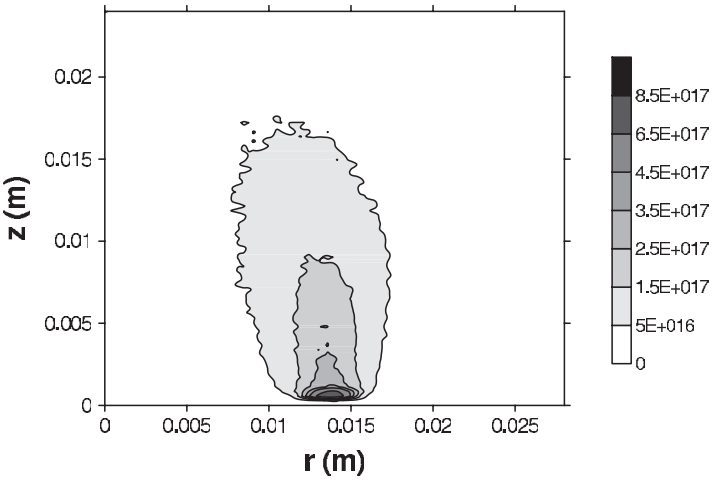


**Figure 2.** Calculated electron density (in $m^{-3}$) at an Ar partial pressure of 1.0 Pa and an $N_2$ partial pressure of 0.26 Pa. Note that the $Y$-axis ($r = 0$) corresponds to the symmetry axis of the cylindrically symmetrical reactor.

$N_2$ pressure. However, in reality, the SEEC values of individual species will probably decrease first, but then remain constant once the poisoning is complete. Nevertheless, the proportion $N(_2)^+/Ar^+$ will increase with $N_2$ flow, and because the SEEC of $N(_2)^+$ is much lower [54] than the SEEC of $Ar^+$ the overall SEEC will indeed decrease with increasing $N_2$ flow.

The SEEC values used, and the calculated currents and voltages as a function of $N_2$ partial pressure are illustrated in figure 1, along with the experimental values.

### *5.2. Calculated electron, ion and atom densities*

The externally applied magnetic field traps the electrons in an area close to the cathode. Most electrons are trapped in the region where the radial magnetic field is at a maximum, causing a peak in the electron density. This is clear from figure 2, presenting the electron density in the simulation area $(r, z)$, for the case of 0.26 Pa $N_2$. Similar profiles for the other $N_2$ partial pressures were obtained, but they are not shown. Indeed, since the SEEC only varies within a limited range due to gas composition (see section 5.1), it will not have a large effect on the electron density.

The localized electrons ionize neutrals, leading to similar density profiles for the $Ar^+$ ions, $N^+$ ions, $N_2^+$ ions and $Ti^+$ ions, as shown in figure 3, for an $N_2$ partial pressure of 0.26 Pa. It is clear from this figure that the $Ar^+$ ions are the dominant positive ions, with a maximum density of $7 \times 10^{17}\ m^{-3}$, which is only slightly lower than the maximum electron density (see figure 2). The $N_2^+$ ions reach a maximum density of about $1.2 \times 10^{17}\ m^{-3}$, which is a factor of almost 6 lower than the $Ar^+$ density, despite the fact that the $N_2$ partial pressure is only a factor of 4 lower than the Ar partial pressure. This is attributed to the fact that the $N_2^+$ ions are lost more efficiently (by dissociative recombination with electrons) than the $Ar^+$ ions. The $N^+$ ion density is still more than an order of magnitude lower (with a maximum density of about $9 \times 10^{15}\ m^{-3}$), which can be explained by the rather low dissociation degree of $N_2$ (i.e. the N atom density is also much lower than the $N_2$ density, as will be shown below). The $Ti^+$ ions have an even lower density, with a maximum of only $1.8 \times 10^{15}\ m^{-3}$, because these species do not originate from the

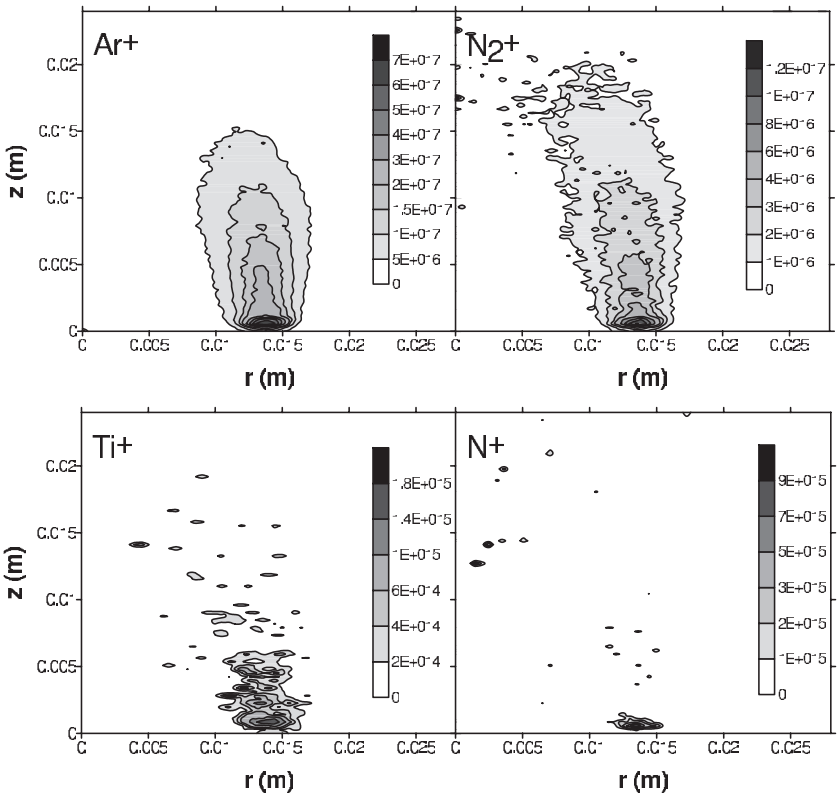


**Figure 3.** Calculated ion densities (in $m^{-3}$) at an Ar partial pressure of 1.0 Pa and a $N_2$ partial pressure of 0.26 Pa. Note that the $Y$-axis ($r = 0$) corresponds to the symmetry axis of the cylindrically symmetrical reactor. (The statistics for $N^+$ and $Ti^+$ are less satisfying due to their lower density and hence lower amount of superparticles.)

background gases, but only from ionization of the sputtered atoms. As most of the fast Ar atoms originate from charge transfer reactions of $Ar^+$ ions, the typical $Ar^+$ ion peak profile appears for the fast Ar atoms as well, see figure 4. Its density is quite high, compared to the ion densities, but it is still two orders of magnitude lower than the overall background Ar gas density, which is of about $2.4 \times 10^{20}\,m^{-3}$. Ti atoms originate from sputtering the cathode target, and therefore, the Ti density has a maximum near the cathode. Its overall density is 3–4 orders of magnitude lower than the Ar atom density. N atoms are also sputtered from the poisoned target, but most N atoms are created in the plasma instead of by sputtering (by reactions (13)–(15), (34) and (36) from table 1). As a consequence, the peak near the cathode is not so pronounced as in the case of the sputtered Ti atoms, and the N density is characterized by a broad profile throughout the discharge. Also, the N density decreases towards the walls, because a SC equal 1 was assumed for N. Because N is not only created by sputtering but also by plasma reactions, the maximum value is almost an order of magnitude higher than the sputtered Ti atom density. Comparing the average N atom density, which is about $1.4 \times 10^{17}\,m^{-3}$, to the $N_2$ molecule density, which is about $6.2 \times 10^{19}\,m^{-3}$, reveals that the dissociation degree is in the order of 0.2%.

To investigate the influence of the $N_2$/Ar gas proportion on the various plasma species, 1d density profiles on a line perpendicular to the cathode at the peak density (i.e. $r = 13.5$ mm)

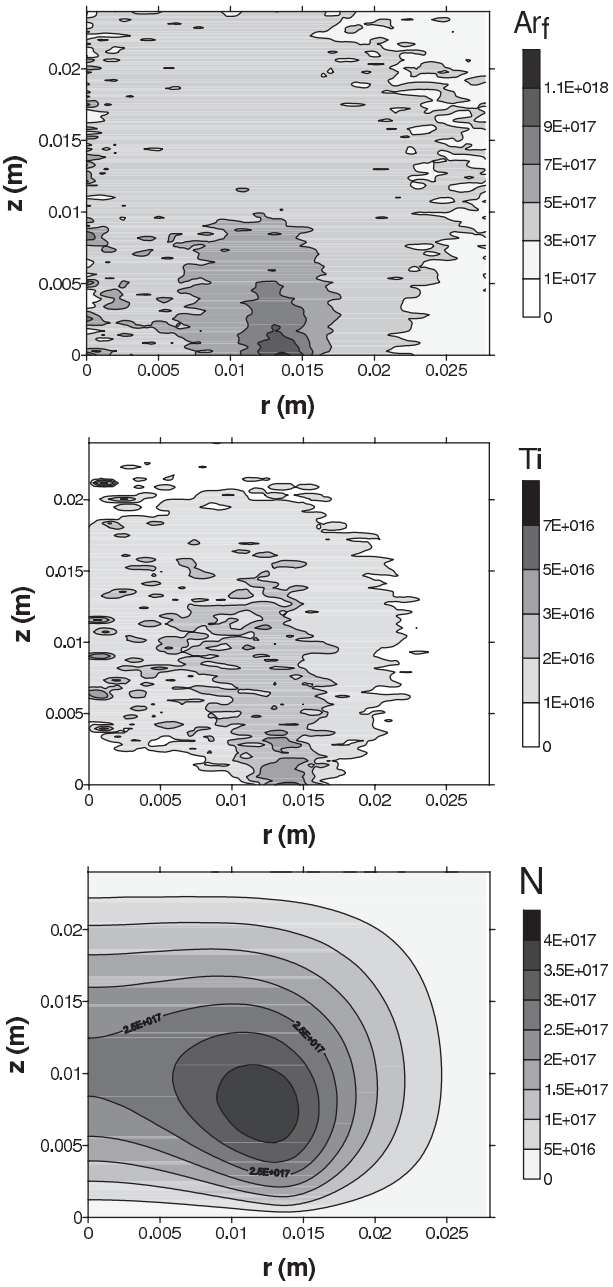


**Figure 4.** Calculated neutral densities (in $m^{-3}$) at an Ar partial pressure of 1.0 Pa and a $N_2$ partial pressure of 0.26 Pa. Note that the $Y$-axis ($r = 0$) corresponds to the symmetry axis of the cylindrically symmetrical reactor. (The statistics for Ti are less satisfying due to its lower density and hence lower amount of superparticles.)

are presented. Figure 5 illustrates the results for the Ti and N atoms. As a consequence of the difference in the Ti sputter yield for a metallic or a poisoned target (as mentioned in section 4.4, and as will be shown below in section 5.4), the Ti density drops significantly upon $N_2$ addition. However, when adding more $N_2$ gas, the Ti density remains constant. The N density rises

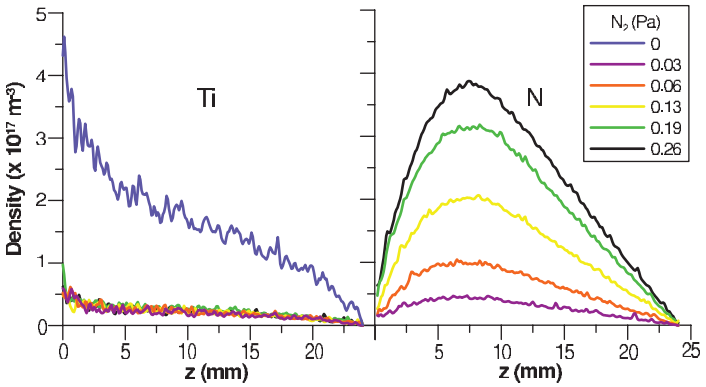


**Figure 5.** Calculated Ti and N atom number densities above the cathode in the $z$-direction (at $r = 13.5$ mm), for different $N_2$ partial pressures as indicated in the legend and at an Ar partial pressure of 1.0 Pa.

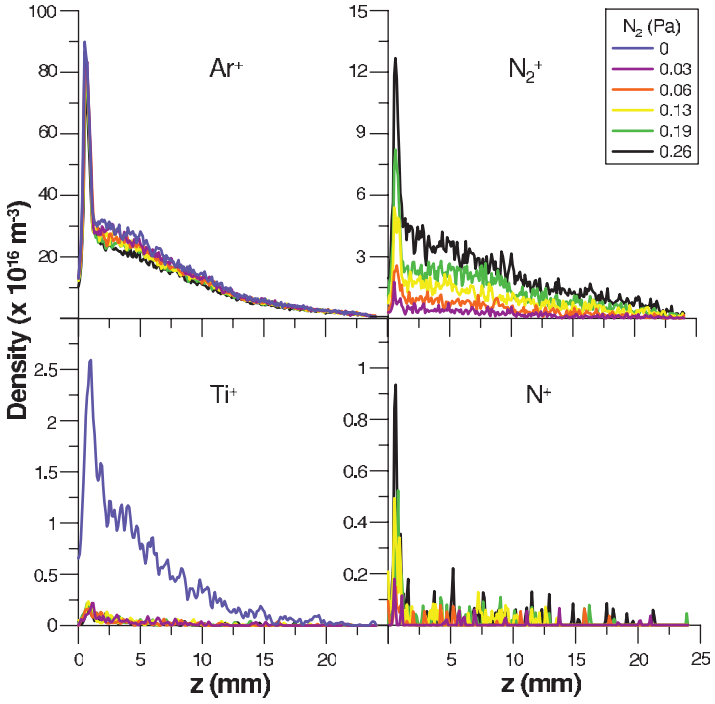


**Figure 6.** Calculated ion densities above the cathode in the $z$-direction (at $r = 13.5$ mm), for different $N_2$ partial pressures as indicated in the legend and at an Ar partial pressure of 1.0 Pa.

logically with $N_2$ gas amount. The explanation for the profiles of the Ti and N densities was given in the paragraph above. The influence of the $N_2$/Ar gas proportion on the 1d ion density profiles is shown in figure 6. When raising the $N_2$ flow, the $N^+$ and $N_2^+$ densities increase and the $Ar^+$ density decreases. This is explained as follows: the charge transfer reaction of $Ar^+$ with $N_2$, which causes the production of $N_2^+$ ions and the loss of $Ar^+$ ions, has a high rate constant (see reaction (21) of table 1). As a consequence, an increased $N_2$ gas amount leads to a higher $N_2^+$

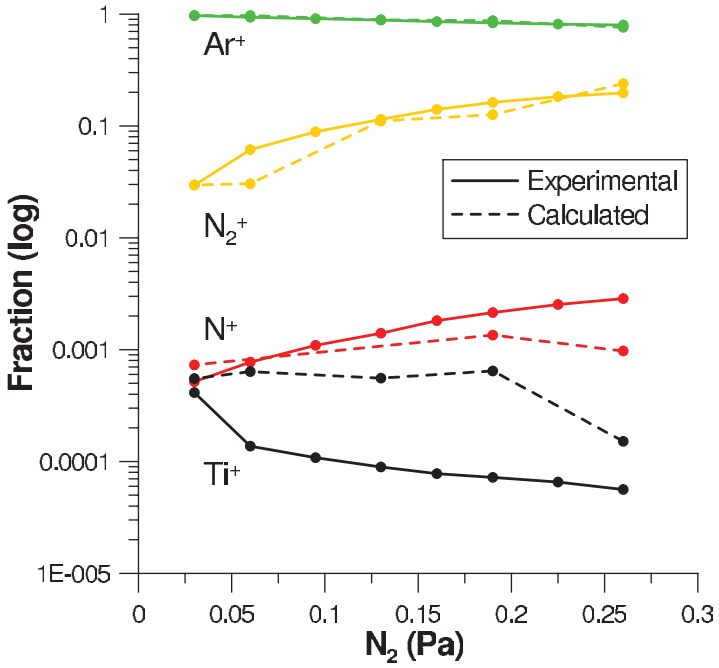


**Figure 7.** Experimental and calculated ion fractions as a function of $N_2$ partial pressure, and at an Ar partial pressure of 1.0 Pa.

density, but to a lower $Ar^+$ density. The $Ti^+$ density drops approximately a factor of 10 when $N_2$ is added, similar to the Ti atom density (figure 5), caused by target poisoning.

Mass spectrometric measurements were carried out to determine the ion fractions at 7 cm from the cathode, for different $N_2$ gas concentrations. However, in order to save computational time, the size of the simulated magnetron reactor was limited to 2.4 cm. Hence, the ion fractions are calculated at 2 cm from the cathode. Nevertheless, it is assumed that the ion proportions will not vary much in the bulk of the plasma. From the measured and calculated ion fractions, presented in figure 7, we conclude that a good agreement with experiment is found, and similar trends as for the ion densities are found. Only for the $Ti^+$ ions is the agreement less satisfactory.

### *5.3. Calculated ion and atom fluxes to the cathode*

The ions accelerate towards the cathode by the applied electric field, where they can sputter the target. Also some neutrals contribute to the sputtering (see below).

In figure 8, particle fluxes to the cathode target, as a function of radial position, are presented for different $N_2$ concentrations. The peak at 13.5 mm is a direct consequence of the maximum in the density profiles (see section 5.2 and figures 3 and 4). When the $N_2$ partial pressure is increased, the $N_2^+$ and $N^+$ fluxes increase and the $Ar^+$ flux decreases, in analogy to their densities (see section 5.2 and figure 6). The $Ti^+$ flux drops approximately a factor of 15 when $N_2$ is added. As was the case for the $Ti^+$ density (see section 5.2), this is a consequence of the lower Ti sputter yield when the target is poisoned (as will be shown in section 5.4). The fast Ar atom flux to the target is rather independent of the $N_2$ amount.

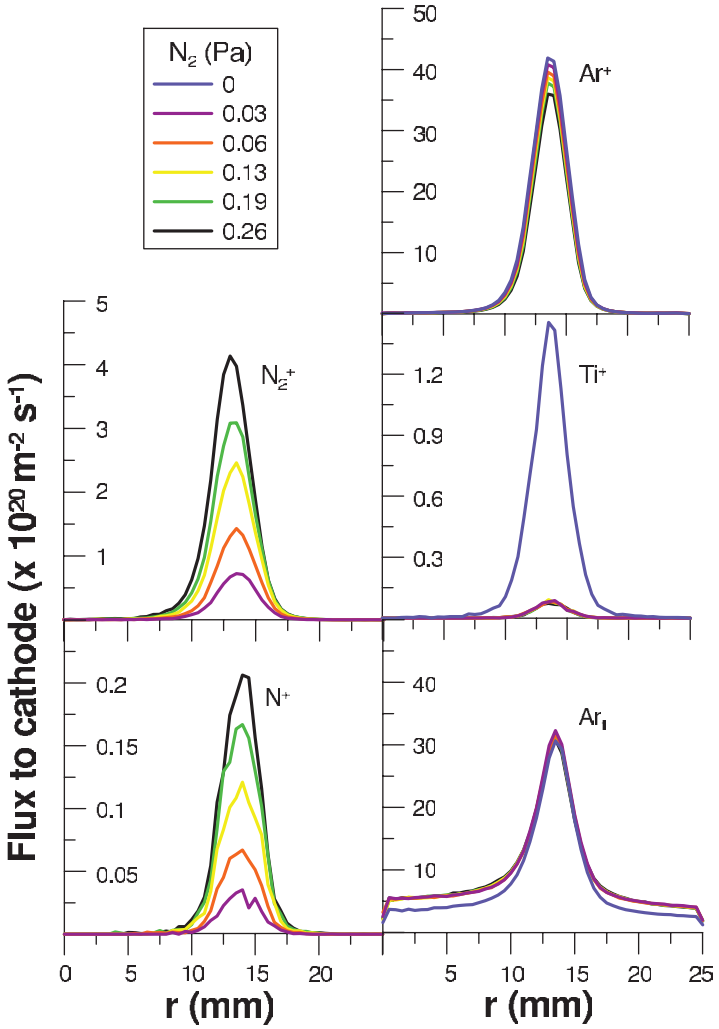


**Figure 8.** Calculated fluxes of the various ions to the cathode for different $N_2$ partial pressures as indicated in the legend and at an Ar partial pressure of 1.0 Pa. Note that the $Y$-axis ($r = 0$) corresponds to the symmetry axis of the cylindrically symmetrical reactor.

### *5.4. Calculated ion and atom contributions to sputtering and total sputter fluxes*

Depending on the magnitude of the fluxes, the corresponding energies, masses and atom numbers, the above-mentioned particles contribute to the sputtering of the target (see equation (9) above). In tables 2 and 3, the relative amount (in %) of Ti and N sputtering, respectively, created by each of these ions and atoms, is summarized.

For both Ti and N, most sputtering is caused by bombarding $Ar^+$ ions, followed by $Ar_f$ atoms. As mentioned before, these $Ar_f$ atoms originate from elastic collisions (reaction (16)), including symmetric charge transfer collisions (reaction (17)), with $Ar^+$ ions [38]. The $N_2^+$ ions only play a role at high $N_2$ partial pressures, and more for sputtering N than Ti, because of the smaller mass differences, and hence the higher sputter yield. The role of $N^+$ and $Ti^+$ ions can be neglected under the investigated conditions, with a contribution of about 0.1–0.5%. The order

**Table 2.** Calculated procentual contribution to the sputtering of Ti (from Ti or $TiN_x$ targets) of the different incident species, as a function of $N_2$ partial pressure, at an Ar partial pressure of 1 Pa.

| Pressure (Pa) | $Ar^+$ | $Ar_f$ | $N_2^+$ | $N^+$ | $Ti^+$ |
|---|---|---|---|---|---|
| 0 | 87.13 | 9.71 | | | 3.00 |
| 0.03 | 87.49 | 11.15 | 0.97 | 0.04 | 0.16 |
| 0.06 | 86.31 | 11.37 | 1.86 | 0.10 | 0.15 |
| 0.13 | 85.26 | 11.92 | 3.24 | 0.19 | 0.17 |
| 0.19 | 84.09 | 10.99 | 4.36 | 0.19 | 0.16 |
| 0.26 | 83.40 | 10.54 | 5.35 | 0.29 | 0.19 |

**Table 3.** Calculated procentual contribution to the sputtering of N (from a $TiN_x$ target) of the different incident species, as a function of $N_2$ partial pressure, at an Ar partial pressure of 1 Pa.

| Pressure (Pa) | $Ar^+$ | $Ar_f$ | $N_2^+$ | $N^+$ | $Ti^+$ |
|---|---|---|---|---|---|
| 0.03 | 89.54 | 8.60 | 1.53 | 0.08 | 0.12 |
| 0.06 | 88.46 | 8.35 | 2.73 | 0.19 | 0.13 |
| 0.13 | 86.62 | 8.10 | 4.75 | 0.31 | 0.10 |
| 0.19 | 85.23 | 7.90 | 6.15 | 0.44 | 0.14 |
| 0.26 | 84.14 | 7.31 | 7.81 | 0.50 | 0.13 |

in contribution is a consequence of the magnitude of the fluxes, as seen in figure 8. In general, raising the $N_2$ partial pressure causes an increase of the $N_2^+$ and $N^+$ contributions and a decrease of the $Ar^+$ contribution to the sputtering of both Ti and N. This can also be explained by the dependance of the $N_2^+$, $N^+$ and $Ar^+$ fluxes on the $N_2$ partial pressure, as seen in section 5.3. From table 2, it is also clear that, when no $N_2$ gas is present, the contribution of $Ti^+$ to sputtering the metallic Ti target is a factor of 15 higher. This is a direct consequence of the $Ti^+$ flux (section 5.3 and figure 8).

The total fluxes of sputtered Ti and N atoms are shown in figure 9. The maxima of the ion and atom fluxes towards the cathode cause a maximum in the sputter flux. This localized erosion of the target creates the so-called 'race track'. When no $N_2$ gas is added, the sputtered Ti flux is approximately a factor of 8 higher than after adding $N_2$, and hence poisoning the target, causing the sputter yield to decrease. Once the target is poisoned, the sputtered Ti flux remains constant and does not drop further upon $N_2$ addition. The sputtered N flux is higher than the sputtered Ti flux due to the higher sputter yield of N (see above, section 4.4). Moreover, in contrast to the Ti flux, the sputtered N flux increases slightly with increasing the $N_2$ partial pressure. This is a consequence of the dependance of the N or Ti sputter yield on the different incoming species. Indeed, sputtering N with $N_2^+$ or $N^+$ ions has a larger yield than with $Ar^+$ ions, whereas sputtering Ti is less dependent on the bombarding ion type. With increasing the $N_2$ flow, the $N_2^+$ and $N^+$ fluxes increase (see section 5.3 and figure 8), causing an enhanced sputtering of N.

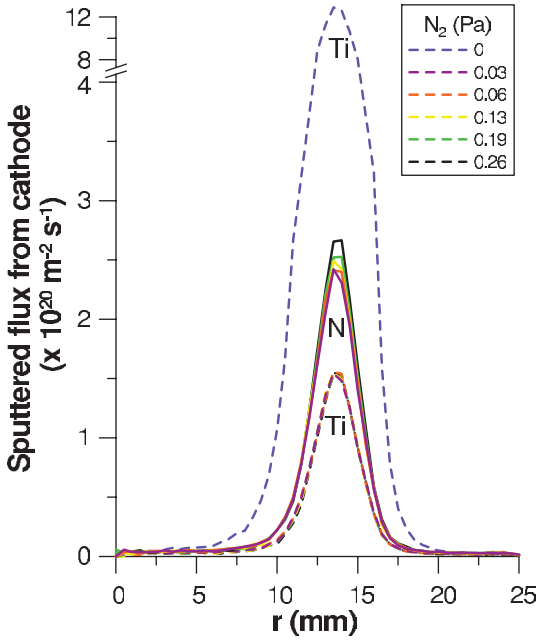


**Figure 9.** Calculated sputtered Ti (dashed lines) and N (solid lines) fluxes from the cathode for different $N_2$ partial pressures as indicated in the legend and at an Ar partial pressure of 1.0 Pa. The lower part of the *Y*-axis is stretched for clarity, because the sputtered Ti flux in pure Ar gas is much higher than in an $Ar/N_2$ mixture. Note that the Y-axis ($r = 0$) corresponds to the symmetry axis of the cylindrically symmetrical reactor.

### *5.5. Calculated Ti and N fluxes to the substrate*

In order to obtain a better insight in the deposition of $TiN_x$ films, the calculated fluxes of Ti and N atoms to the substrate are presented in figure 10.

The Ti flux to the anode drops when $N_2$ is added, and remains constant afterwards, in correspondance to the sputtered Ti flux (see section 5.4 and figure 9). The Ti flux to the anode is characterized by a similar radial peak profile as the sputtered Ti flux, implying that the deposited Ti in the film will be non-uniform. The broadening of the peak profile is a consequence of diffusion of the sputtered Ti atoms through the plasma. In analogy to the sputtered fluxes (see section 5.4 and figure 9), the N flux to the anode is higher than the Ti flux almost everywhere. The N flux has lost its radial peak profile, as was also clear from the N density (see section 5.2 and figure 4), because more N is created by plasma reactions than by sputtering. The N flux increases with $N_2$ amount, similar to the N density (see figure 5).

When the absolute values of the fluxes of Ti and N to the substrate are compared (figure 10), and taking into account the assumed SCs of 0.5 and 1, respectively, most of the deposited $TiN_x$ film would have a stoichiometry $x$ much greater than 1. This implies that the assumed SC of N atoms must be much lower, probably of the order of 0.1, as reported in [55]. On the other hand, as stated in [26], the effective SC of a species will be a function of the coverage of the different species on the deposited film. Indeed, with increasing N coverage, the effective $SC_N$ will be lower. Therefore, it would be advisable to couple our PIC/MCC model to a surface model, such as [27, 56], to account for this lower effective SC of N.

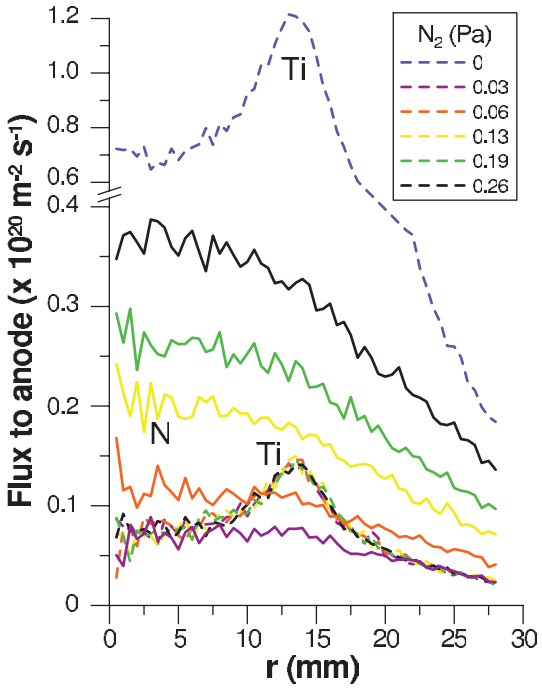


**Figure 10.** Calculated Ti (dashed lines) and N (solid lines) fluxes to the anode for different $N_2$ partial pressures as indicated in the legend and at an Ar partial pressure of 1.0 Pa. The lower part of the $Y$-axis is stretched for clarity, because the Ti flux to the anode in pure Ar gas is much higher than in an $Ar/N_2$ mixture. Note that the $Y$-axis ($r = 0$) corresponds to the symmetry axis of the cylindrically symmetrical reactor.

## 6. Conclusion

To simulate the physical processes in a magnetron discharge during reactive sputter deposition, a 2d3v PIC/MCC modelling approach was applied. With this model, we are able to calculate in detail the densities and fluxes of the various species in the whole reactor. The model was validated by comparing calculated ion fractions to mass spectrometric measurements. Although this modelling approach is very accurate and self-consistent, it suffers from a long calculation time. Consequently, it is not so suitable for large reactors. However, its precise results can be used to understand certain mechanisms, and hence to improve simpler, but faster models, such as fluid and analytical models, which can deal with larger reactors.

This model accounts for poisoning of the titanium target when $N_2$ gas is added, using $N_2$ pressures for which the target is completely poisoned. However, the poisoning process of the target at low $N_2$ pressures, i.e. the hysteresis behaviour, is not described in the model. Reaching steady state at low $N_2$ pressures takes several seconds to minutes, and therefore a PIC/MCC approach will not be suitable.

With respect to the deposition of $TiN_x$ films, a stoichiometry $x$ much larger than one is predicted, when SCs of Ti and N of 0.5 and 1, respectively, are used. Therefore, the effective SC of N will probably be much lower than 1, and will be a function of the film coverage. In the future, we plan to couple the PIC/MCC model to a surface model to account for this. Also,

the sticking of molecular $N_2$ gas will be included in the surface model, because $N_2$ can also contribute to the deposition of the $TiN_x$ film due to its high density.

Nevertheless, this model is already able to provide accurate information on the processes that occur in the plasma. It can be used as an extension or even validation for experiments and simple models, to get a step closer to a complete view of reactive magnetron sputter deposition.

In the future, this PIC/MCC model can be extended to other reactive gases (e.g. $Ar/O_2$) or combinations (e.g. $Ar/N_2/O_2$), and to other electric (e.g. rf, pulsed dc, maybe HIPIMS) or magnetic (e.g. unbalanced) configurations.

## Acknowledgments

EB is indebted to the University of Antwerp for financial support. SM is indebted to the FWO-Flanders for his postdoctoral fellowship. The authors thank Professor W Möller for interesting discussions on the plasma–surface interactions. The computer facility CALCUA from the University of Antwerp is acknowledged.

## References

[1] Waits R K 1978 Planar magnetron sputtering *J. Vac. Sci. Technol.* **15** 179
[2] Guo Q X, Yoshitugu M, Tanaka T, Nishio M and Ogawa H 2005 Microscopic investigations of aluminum nitride thin films grown by low-temperature reactive sputtering *Thin Solid Films* **483** 16
[3] Figueroa U, Salas O and Oseguera J 2004 Production of AlN films: ion nitriding versus PVD coating *Thin Solid Films* **469–470** 295
[4] Mahmood A, Machorro R, Muhl S, Heiras J, Castillon F F, Farias M H and Andrade E 2003 Optical and surface analysis of dc-reactive sputtered AlN films *Diam. Relat. Mater.* **12** 1315
[5] Mahieu S, Ghekiere P, De Winter G, De Gryse R, Depla D, Van Tendeloo G and Lebedev O I 2006 Biaxially aligned titanium nitride thin films deposited by reactive unbalanced magnetron sputtering *Surf. Coat. Technol.* **200** 2764
[6] Fu Y, Du H and Zhang S 2003 Functionally graded TiN/TiNi shape memory alloy films *Mater. Lett.* **57** 2995
[7] de Pinho Alves Neto J, Giacomelli C, Klein A N, Muzart J L R and Spinelli A 2005 Electrochemical stability of magnetron-sputtered Ti films on sintered and sintered/plasma nitrided Fe–1.5% Mo alloy *Surf. Coat. Technol.* **191** 206
[8] Alsaran A, Celik A and Karakan M 2005 Structural, mechanical and tribological properties of duplex-treated AISI 5140 steel *Mater. Charact.* **54** 85
[9] Szikora B 1998 Background of the titanium nitride deposition *Vacuum* **50** 273
[10] Safi I 2000 A novel reactive magnetron sputtering technique for producing insulating oxides of metal alloys and other compound thin films *Surf. Coat. Technol.* **135** 48
[11] Koski K, Holsa J, Juliet P, Wang Z H, Aimo R and Pischow K 1999 Characterisation of aluminium oxide thin films deposited on polycarbonate substrates by reactive magnetron sputtering *Mater. Sci. Eng.* B **65** 94
[12] Ghekiere P, Mahieu S, De Winter G, De Gryse R and Depla D 2005 Scanning electron microscopy study of the growth mechanism of biaxially aligned magnesium oxide layers grown by unbalanced magnetron sputtering *Thin Solid Films* **493** 129
[13] Bartzsch H, Gloss D, Bocher B, Frach P and Goedicke K 2003 Properties of $SiO_2$ and $Al_2O_3$ films for electrical insulation applications deposited by reactive pulse magnetron sputtering *Surf. Coat. Technol.* **174** 774

[14] Kelly P J, Beevers C F, Henderson P S, Arnell R D, Bradley J W and Backer H 2003 A comparison of the properties of titanium-based films produced by pulsed and continuous dc magnetron sputtering *Surf. Coat. Technol.* **174–175** 795
[15] O'Brien J and Kelly P J 2001 Characterisation studies of the pulsed dual cathode magnetron sputtering process for oxide films *Surf. Coat. Technol.* **142** 621
[16] Henderson P S, Kelly P J, Arnell R D, Backer H and Bradley J W 2003 Investigation into the properties of titanium based films deposited using pulsed magnetron sputtering *Surf. Coat. Technol.* **174** 779
[17] Depla D and Mahieu S 2008 *Reactive Sputter Deposition* (Berlin: Springer)
[18] Buyle G, Depla D, Eufinger K, Haemers J, De Bosscher W and De Gryse G 2004 Simplified model for the dc planar magnetron discharge *Vacuum* **74** 353
[19] Wadley H N G, Zhou X W, Jhonson R A and Neurock M 2001 Mechanisms, models and methods of vapor deposition *Prog. Mater. Sci.* **46** 329
[20] Kolev I and Bogaerts A 2004 Numerical models of the planar magnetron glow discharges *Contrib. Plasma Phys.* **44** 582
[21] Bogaerts A, Van Straaten M and Gijbels R 1995 Description of the thermalisation process of the sputtered atoms in a glow discharge using a three-dimensional Monte Carlo method *J. Appl. Phys.* **77** 1868
[22] Birdsall C K and Langdon A B 1991 *Plasma Physics via Computer Simulations* (Bristol: Institute of Physics Publishing)
[23] Kolev I and Bogaerts A 2006 Detailed numerical investigation of a dc sputter magnetron *IEEE Trans. Plasma Sci.* **34** 886
[24] Kolev I and Bogaerts A 2006 PIC/MCC numerical simulation of a dc planar magnetron *Plasma Process. Polym.* **3** 127
[25] Berg S and Nyberg T 2005 Fundamental understanding and modeling of reactive sputtering processes *Thin Solid Films* **476** 215
[26] Möller W and Güttler D 2007 Modelling of plasma-target interaction during reactive magnetron sputtering of TiN *J. Appl. Phys.* **102** 094501
[27] Depla D, Heirwegh S, Mahieu S and De Gryse R 2007 Towards a more complete model for reactive magnetron sputtering *J. Phys. D: Appl. Phys.* **40** 1957
[28] Pflug A, Szyszka B and Niemann J 2003 Simulation of reactive sputtering kinetics in real in-line processing chambers *Thin Solid Films* **442** 21
[29] Nanbu K, Mitsui K and Kondo S 2000 Self-consistent particle modelling of dc magnetron discharges of an $O_2$/Ar mixture *J. Phys. D: Appl. Phys.* **33** 2274
[30] Depla D and De Gryse R 2001 Influence of oxygen addition on the target voltage during reactive sputtering of aluminium *Plasma Sources Sci. Technol.* **10** 547
[31] Depla D, Tomaszewski H, Buyle G and De Gryse R 2006 Influence of the target composition on the discharge voltage during magnetron sputtering *Surf. Coat. Technol.* **201** 848
[32] Bultinck E, Kolev I, Bogaerts A and Depla D 2007 The importance of an external circuit in a particle-in-cell/Monte Carlo collisions model for a direct current planar magnetron *J. Appl. Phys.* **103** 013309
[33] Window B and Savvides N 1986 Charged particle fluxes from planar magnetron sputtering sources *J. Vac. Sci. Technol.* A **4** 196
[34] Kolev I, Bogaerts A and Gijbels R 2005 Influence of electron recapture by the cathode upon the discharge characteristics in dc planar magnetrons *Phys. Rev.* E **72** 056402
[35] Vahedi V, Birdsall C K, Lieberman M A, DiPeso G and Rognlien T D 1993 Verification of frequency scaling laws for capacitive radio-frequency discharges using two-dimensional simulations *Phys. Fluids* B **5** 2719
[36] Acton F S 1991 *Numerical Methods that Work* (Washington: Mathematical Association of America)
[37] Boris J 1970 Relativistic plasma simulation—optimization of a hybrid code *4th Conf. on the Numerical Simulation of Plasma, Naval Research Laboratory, Washington, DC* pp 3–67
[38] Phelps A V 1994 The application of scattering cross sections to ion flux models in discharge sheaths *J. Appl. Phys.* **76** 747

[39] Nanbu K and Kitatani Y 1995 An ion–neutral collision model for particle simulation of glow discharge *J. Phys. D: Appl. Phys.* **28** 324
[40] Georgieva V, Bogaerts A and Gijbels R 2003 Particle-in-cell/Monte Carlo simulation of a capacitively coupled radio frequency $Ar/CF_4$ discharge: effect of gas composition *J. Appl. Phys.* **93** 2369
[41] Nanbu K 2000 Probability theory of electron–molecule, ion–molecule, molecule–molecule and Coulomb collisions for particle modeling of materials processing plasmas and gases *IEEE Trans. Plasma Sci.* **28** 971
[42] Lieberman M A and Lichtenberg A J 1994 *Principles of Plasma Discharges and Materials Processing* (New York: Wiley)
[43] Temkin A 1978 Internuclear dependence of the polarizability of $N_2$ *Phys. Rev.* A **17** 1232
[44] Matsunami N, Yamamura Y, Itikawa Y, Itoh N, Kazumata Y, Miyagawa S, Morita K, Shimizu R and Tawara H 1984 Energy dependence of the ion-induced sputtering yields of monatomic solids *At. Data Nucl. Data Tables* **31** 1
[45] Hirschfelder J O, Curtiss C F and Bird R B 1964 *Molecular Theory of Gases and Liquids* (New York: Wiley)
[46] Zhen S and Davies G J 1983 Calculation of the Lennard–Jones n–m potential energy parameters for metals *Phys. Status Solidi* a **78** 595
[47] Svehla R A 1962 Estimated viscosities and thermal conductivities of gases at high temperatures *National Aeronautics and Space Administraion (NASA), Technical Report* p R132
[48] Lewis M A, Glocker D A and Jorne J 1989 Measurements of secondary-electron emission in reactive sputtering of aluminium and titanium nitride *J. Vac. Sci. Technol.* A **7** 1019
[49] Oechsner H 1978 Electron yields from clean polycrystalline metal surfaces by noble-gas-ion bombardment at energies around 1 keV *Phys. Rev.* B **17** 1052
[50] Depla D, Li X Y, Mahieu S and De Gryse R 2008 Determination of the effective electron emission yields of compound materials *J. Phys. D: Appl. Phys.* **41** 202003
[51] Depla D, Heirwegh S, Mahieu S, Haemers J and De Gryse R 2007 Understanding the discharge voltage behavior during reactive sputtering of oxides *J. Appl. Phys.* **101** 013301
[52] Mahieu S, Van Aeken K, Depla D, Smeets D and Vantomme A 2008 Dependence of the sticking coefficient of sputtered atoms on the target–substrate distance *J. Phys. D: Appl. Phys.* **41** 152005
[53] Kolev I 2007 Particle-in-cell–Monte Carlo collisions simulations for a direct current planar magnetron discharge *PhD Thesis* University of Antwerp
[54] Baragiola R A, Alonso E V, Ferron J and Olivaflorio A 1979 Ion-induced electron-emission from clean metals *Surf. Sci.* **90** 240
[55] Mao D, Tao K and Hopwood J 2002 Ionized physical vapor deposition of titanium nitride: plasma and film characterization *J. Vac. Sci. Technol.* A **20** 379
[56] Kubart T, Kappertz O, Nyberg T and Berg S 2006 Dynamic behaviour of the reactive sputtering process *Thin Solid Films* **515** 421
[57] ftp://jila.colorado.edu/collision_data/electronneutral/hayashi.txt
[58] Phelps A V and Petrovic Z Lj 1999 Cold-cathode discharges and breakdown in argon: surface and gas phase production of secondary electrons *Plasma Sources Sci. Technol.* **8** R21
[59] Mason N J and Newell W R 1987 Total cross sections for metastable excitation in rare gases *J. Phys. B: At. Mol. Phys.* **20** 1357
[60] Eggarter E 1975 Comprehensive optical and collision data for radiation action. ii. $Ar^*$ *J. Chem. Phys.* **62** 833
[61] Hyman H A 1979 Electron-impact ionization cross sections for excited states of the rare gases (Ne, Ar, Kr, Xe), cadmium and mercury *Phys. Rev.* A **20** 855
[62] Hyman H A 1978 Electron-impact excitation of metastable argon and krypton *Phys. Rev.* A **18** 441
[63] Vriens L 1964 Calculation of the absolute ionisation cross sections of He, He*, $He^+$, Ne, Ne*, $Ne^+$, Ar, Ar*, Hg and Hg* *Phys. Lett.* **8** 260
[64] ftp://jila.colorado.edu/collision_data

[65] Itikawan Y, Hayashi M, Ichimura A, Onda K, Sakimoto K, Takayanagi K, Nakamura M, Nishimura H and Takayanagi T 1986 Cross sections for collisions of electrons and photons with nitrogen molecules *J. Phys. Chem. Ref. Data* **15** 985

[66] Georgieva V, Bogaerts A and Gijbels R 2003 Numerical study of $Ar/CF_4/N_2$ discharges in single- and dual-frequency capacitively coupled plasma reactors *J. Appl. Phys.* **94** 3748

[67] Phelps A V 1991 Cross sections and swarm coefficients for nitrogen ions and neutrals in $N_2$ and argon ions and neutrals in Ar for energies from 0.1 eV to 10 keV *J. Phys. Chem. Ref. Data* **20** 557

[68] Bogaerts A and Gijbels R 1996 Role of sputtered Cu atoms and ions in a direct current glow discharge: combined fluid and Monte Carlo model *J. Appl. Phys.* **79** 1279

[69] Henriques J, Tatarova E, Guerra V and Ferreira C M 2002 Wave driven $N_2$–Ar discharge. I. Self-consistent theoretical model *J. Appl. Phys.* **91** 5622

[70] Ferreira C M and Ricard A 1983 Modelling of the low-pressure argon positive column *J. Appl. Phys.* **54** 2261

[71] Ferreira C M, Loureiro J and Ricard A 1985 Populations in the metastable and the resonance levels of argon and stepwize ionization effects in a low-pressure argon positive column *J. Appl. Phys.* **57** 82

[72] Riseberg L A, Parks W F and Schearer L D 1973 Penning ionization of Zn and Cd by noble-gas metastable atoms *Phys. Rev.* A **8** 1962

[73] Tachibana K 1986 Excitation of the $1s_5$, $1s_4$, $1s_3$, $1s_2$ levels of argon by low-energy electrons *Phys. Rev.* A **34** 1007

[74] Phelps A V, Greene C H and Burke J P Jr 2000 Collision cross sections for argon atoms with argon atoms for energies from 0.01 eV to 10 keV *J. Phys. B: At. Mol. Opt. Phys.* **33** 2965

[75] Phelps A V and Jelenkovic B M 1988 Excitation and breakdown of Ar at very high ratios of electric field to gas density *Phys. Rev.* A **38** 2975

[76] Robinson R S 1979 Energetic binary collisions in rare gas plasmas *J. Vac. Sci. Technol.* **16** 185